arXiv:1611.04991v1 [physics.flu-dyn] 15 Nov 2016

Local dissipation limits the dynamics of impacting droplets on smooth and rough substrates

Yuli Wang,[1, 2, a)] Gustav Amberg,[3, 1, b)] and Andreas Carlson[2, c)]

[1)] *Department of Mechanics*

The Royal Institute of Technology, 100 44 Stockholm, Sweden

[2)] *Department of Mathematics*

University of Oslo, 0851 Oslo, Norway

[3)] *Södertörn University, 14189 Huddinge, Sweden*

(Dated: 16 November 2016)

A droplet that impacts onto a solid substrate deforms in a complex dynamics. To extract the principal mechanisms that dominate this dynamics we deploy numerical simulations based on the phase field method. Direct comparison with experiments suggests that a dissipation local to the contact line limits the droplet spreading dynamics and its scaled maximum spreading radius $\beta_{\max}$. By assuming linear response through a drag force at the contact line, our simulations rationalize experimental observations for droplet impact on both smooth and rough substrates, measured through a single contact line friction parameter μ_f. Moreover, our analysis shows that at low and intermediate impact speeds dissipation at the contact line limits the dynamics and we describe $\beta_{\max}$ by the scaling law $\beta_{\max} \sim (Re\mu_l/\mu_f)^{1/2}$ that is a function of the droplet viscosity (μ_l) and its Reynolds number (Re).

[a)] yuli@mech.kth.se

[b)] gustav.amberg@sh.se

[c)] acarlson@math.uio.no

I. INTRODUCTION

Impact of liquid droplets onto a solid substrate is essential to applications such as spray coating[1], ink-jet printing[2], additive manufacturing[3] and pesticide deposition[4]. Upon impact with the substrate the droplet deforms in a complex dynamics, where a gas film can become trapped underneath the droplet[5–12] and as it spreads create a splash by droplet ejection at the tip of its spreading front[13–17]. The droplet deformation and spreading is typically driven by its inertia and hindered by viscous and surface tension forces. Two non-dimensional numbers are particularly relevant to characterize the dynamics, which is the Reynolds number $Re = \rho_\mathrm{l} V_i 2R/\mu_\mathrm{l}$ giving the ratio between inertia and viscous forces and the Weber number $We = \rho_\mathrm{l} V_i^2 2R/\sigma$ which gives the ratio between inertia and surface tension forces. σ is the surface tension coefficient of the gas-liquid, ρ_l is the liquid density, μ_l is the liquid viscosity and V_i is the droplet impact speed. Besides inertia, viscosity and surface tension, we hypothesize and show that a dissipation local to the contact line can limit the droplet dynamics on both smooth and rough substrates.

One parameter that describes the droplet impact dynamics and is typically quantified is the spreading factor $\beta(t) = R(t)/R$, where $R(t)$ is the droplet spreading radius, R is the initial droplet radius and $\beta_\mathrm{max} = \max(\beta(t))$, see Fig.1. Two primary regimes have been identified to describe β_max; an inertia-viscous regime where $\beta_\mathrm{max} \sim Re^{\frac{1}{5}}$[18,19] and an inertia-capillary regime where $\beta_\mathrm{max} \sim We^{\frac{1}{2}}$[20,21]. A single law has been derived to connect these two regimes $\beta_\mathrm{max} Re^{-\frac{1}{5}} \sim f(WeRe^{-\frac{2}{5}})$[22], which has rationalized experiments for a wide range of Re and We numbers[23]. Other scaling laws for β_max with different exponents for Re and We have been proposed[24–30], which include additional effects such as the substrate wettability. A detailed description of these different scaling laws can be found in the recent review by Josserand and Thoroddsen[31]. However, none of these scaling laws describe β_max at the low impact speeds as they predict $\beta_\mathrm{max} \to 0$ as $V_\mathrm{i} \to 0$, which is not true for any case with an equilibrium contact angle $\theta_\mathrm{e} < 180°$. To mitigate this artifact the maximum spreading radius β_0 for $V_\mathrm{i} = 0$ has been included into the analysis $\sqrt{\beta_\mathrm{max}^2 - \beta_0^2} = Re^{\frac{1}{5}} We^{\frac{1}{2}}/(A + We^{\frac{1}{2}})$ that agrees favorably with experimental data for both low and high impact speeds[32], where A is an ad-hoc fitting parameter.

Substrate roughness is another parameter that can influence the droplet impact dynamics[33–37]. Droplet impact on regular micro-textured substrates[33,34,38] show that β_max is influenced by

the substrate topography. Even a substrate with small aspect ratio roughness hinders droplet spreading[35], although the effect becomes less pronounced.

In this work we focus on describing $\beta(t)$ and $\beta_{\max}$ in the regime of non-splashing droplets[31,39] i.e. small and intermediate impact speed. We show that as in a spontaneous droplet spreading process[40,41], a detailed description of the physical processes at the contact line must be included to accurately describe the interface dynamics. Numerical experiments based on the phase field method and the Navier Stokes equations show that friction local to the contact line limits the dynamics and generates a significant dissipation. We treat the contact line friction parameter μ_f as a material property for each combination of air-liquid-solid, which should be independent of the impact speed. We determine the magnitude of μ_f by directly comparing the numerical simulations with several independent experiments[23,25,32,34,35]. Our assumption of linear response through a Stokes-like drag at the contact line shows that the simulations can accurately reproduce experimental observations. We further extend our analysis to rough substrates and rationalize the differences in the dynamics compared with smooth substrates. Finally, we show that the regime where the principal dissipation is local to the contact line is described by a scaling law based on the contact line friction parameter μ_f.

A. Models and Methods

We describe the multiphase system by using the phase field method[42], which considers the two binary phases (gas liquid) as a mixture. The mathematical model is composed of the Cahn-Hilliard equation[43] Eq.(1,2), which is coupled with the Naiver-Stokes equations Eq.(3,4) for an incompressible fluid flow[42];

$$\frac{\partial C}{\partial t} + \mathbf{u} \cdot \nabla C = \gamma \nabla^2 \phi \tag{1}$$

$$\phi = -\frac{3}{2\sqrt{2}}\sigma \left(\epsilon \nabla^2 C - \frac{C^3 - C}{\epsilon} \right) \tag{2}$$

$$\rho(C) \left(\frac{\partial \mathbf{u}}{\partial t} + (\mathbf{u} \cdot \nabla)\mathbf{u} \right) = -\nabla P + \nabla \cdot (\mu(C)(\nabla \mathbf{u} + (\nabla \mathbf{u}))^T) + \phi \nabla C \tag{3}$$

$$\nabla \cdot \mathbf{u} = 0. \tag{4}$$

$C = C(r, z, t)$ is an order parameter that varies smoothly from $C = -1$ (gas) to $C = 1$ (liquid) between the two immiscible phases and $|C| < 1$ indicates that the interfacial region

that has a finite thickness ϵ. $\phi = \phi(r, z, t) = \delta F(r, z, t)/\delta C$ is the chemical potential, given by the variation of the systems postulated free energy $F(r, z, t)$ that has an interfacial and bulk free energy term. The free energy is required to reduce with time i.e. $\gamma > 0$ and γ is the mobility factor that controls the interfacial diffusion. $\mathbf{u} = \mathbf{u}(r, z, t)$ is the velocity, $P = P(r, z, t)$ is the pressure, whereas the density $\rho(C) = (1 + C)\rho_{\rm l}/2 + (1 - C)\rho_{\rm g}/2$ and the viscosity $\mu(C) = (1 + C)\mu_{\rm l}/2 + (1 - C)\mu_{\rm g}/2$ are interpreted as function of C. The air surrounding the droplet is assumed at atmospheric pressure with a density $\rho_{\rm g} = 1.23{\rm kg/m}^3$ and a viscosity $\mu_{\rm g} = 1.81 \times 10^{-5}$Pa.s. The material properties of the droplet, along with the impact speeds, equilibrium contact angles and range of simulated Re numbers and We numbers are listed in Table I.

All simulations are performed with a no-slip boundary condition for the velocities at the solid substrate ($\mathbf{u} = 0$) and all other boundaries are assumed to be in contact with ambient air at constant pressure ($P = 0$) and with no-flux of the chemical potential ($\nabla\phi \cdot \mathbf{n} = 0$ with $\mathbf{n}$ as the boundary normal). To model the contact line dynamics we use the non-equilibrium boundary condition[44],

$$\frac{2\sqrt{2}}{3}\sigma\epsilon\nabla C \cdot {\rm n} + \sigma\cos(\theta_{\rm e})g'(C) = -\mu_f\epsilon\frac{\partial C}{\partial t} \tag{5}$$

where μ_f is interpreted as a friction factor at the contact line and $g(C) = -2/4 - 3/4C + 1/4C^3$ provides a transition for the dry (gas-solid) or wet (liquid-solid) substrate surface tension. For $\mu_f = 0$ we assume local equilibrium at the contact line and the interface adopts the equilibrium contact angle $\theta_{\rm e}$, but if $\mu_f > 0$ the contact angle becomes dynamic and allowed to deviate from $\theta_{\rm e}$.

We use the following scaling; $\mu^*(C) = \mu(C)/\mu_{\rm l}, \rho^*(C) = \rho(C)/\rho_{\rm l}, \mathbf{u}^* = \mathbf{u}/V_{\rm i}, t^* = tV_{\rm i}/R, P^* = PR/(\mu_{\rm l}V_{\rm i}), \phi^* = \phi 2\sqrt{2}\epsilon/(3\sigma)$ to make Eq.(1)-Eq.(5) non-dimensional, where the superscript $*$ denotes non-dimensional variables. In addition to the Reynolds number Re four non-dimensional numbers appear in the equations; the Capillary number $Ca = We/Re = V_{\rm i}\mu_{\rm l}/\sigma$ gives the ratio of the viscous force to the surface tension force, the non-dimensional friction parameter $D_{\rm w} = (\epsilon\mu_f V_{\rm i})/(R\sigma)$ gives the ratio of the contact line friction force to the surface tension force, the Cahn number $Cn = \epsilon/R = 0.005$ gives the ratio of the interface thickness and the droplet radius, and the Péclet number $Pe = 2\sqrt{2}V_{\rm i}\epsilon R/(3\sigma\gamma) = 100$ gives the ratio of advection to diffusion. Both Cn and Pe are fixed in all of our simulations such that the results satisfy the sharp interface criterion[45,46], $\epsilon = 0.005R$ and

$\gamma = (2\sqrt{2}V_{\rm i}\epsilon R)/(300\sigma)$. The contour line $C = 0$ is interpreted as the droplet interface and used to extract $\beta(t), \beta_{\rm max}$ and $\theta_{\rm d}(t)$.

The numerical simulations are performed with FemLego[47], a symbolic finite element toolbox that solves partial differential equations. All simulations are performed in an axi-symmetric coordinate system where the domain extends $10R$ in the r direction and $5R$ in the z direction. An adaptive mesh refinement method is used to enable a high resolution of the interface with a minimum mesh size of $\Delta r \approx \Delta z \approx 0.001R$, which resolves the interface with $Cn/\Delta r \approx 5$ cells. The droplet's center of mass is initialized at a height $z = 1.5R$ from the solid substrate and the dynamic contact angle $\theta_{\rm d}(t)$ is measured at a height of $z = 100\mu$m using linear interpolation along $C = 0$ similar to the method used to in the experimental analysis that we are directly comparing against[32].

The phase field method has previously been used with success to simulate droplet impact dynamics[48,49] to quantify the early spreading and bubble entrapment, in accordance with experimental observations[50]. However, none of these account for a dynamic contact angle treatment in Eq.(5) with $\mu_f > 0$ or quantify the maximum spreading radius of the droplet, which we will show are two intertwined processes needed to rationalize the impact dynamics of droplets on smooth and rough solid substrates.

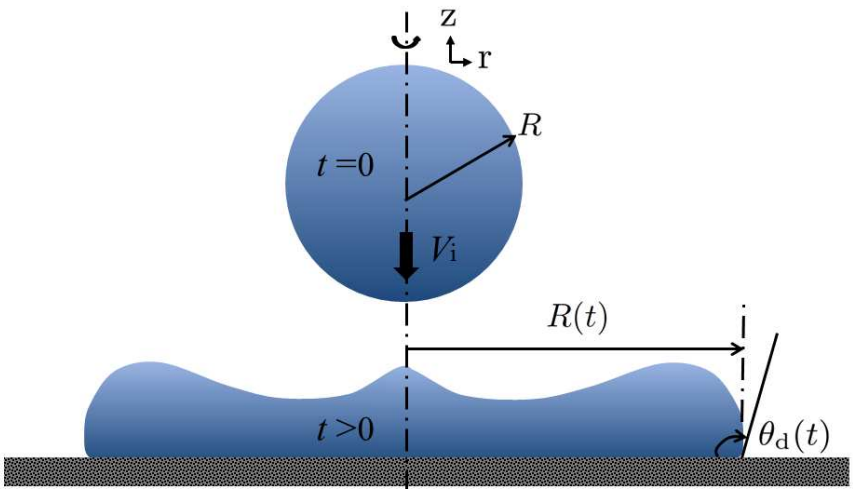

FIG. 1. Sketch of the axi-symmetric computational domain and the droplets initial condition with R the initial droplet radius and V_i the impact speed. The spreading radius $R(t)$ and the apparent dynamic contact angle $\theta_{\rm d}(t)$ is illustrated as the droplet has spread onto the solid substrate.

TABLE I. Simulated material properties and droplet impact conditions on substrates with different equilibrium contact angles (θ_{e}([steel, stainless steel, aluminium,grooved stainless steel]$_{\mathrm{air-water}}$)=[61°, 90°, 94°, 130°] and θ_{e}([steel]$_{\mathrm{air-glycerol/water}}$)=[52°]).

	$\rho_l(\mathrm{kg}\cdot\mathrm{m}^{-3})$	μ_{l}(Pa.s)	$\sigma(\mathrm{N}\cdot\mathrm{m}^{-1})$	R(mm)	V_i(m/s)	$\theta_e(^\circ)$	Re	We
water	1000	0.001	0.073	1	0.28-4.85	61,90,94,130	320-10^4	0.6-664
glycerol-water	1158	0.01	0.068	0.92	0.19-9.28	52	40-1956	1-2653

II. RESULTS AND DISCUSSIONS

A. Droplet impact on smooth substrate

Phase field simulations of droplets that spontaneously spread onto a solid substrate has shown that in order to accurately describe the contact line dynamics a local dissipation by using $\mu_f > 0$ in Eq.5 is required[41]. The mathematical form of Eq.5 comes from the assumption of linear response with a reduction of the free energy in time, and can be interpreted as a Stokes-like drag at the contact line. We interpret this wall-interface friction parameter μ_f as a physical property that depends on the combination of the gas-liquid-solid. We hypothesize that parts of the parameter space that compose the droplet impact dynamics can only be described with an accurate local treatment of the dynamic contact angle through μ_f.

Since μ_f is not known a-priori we determine its magnitude by directly comparing simulations with experiments[25,32], where μ_f is identified as the best-match with $\beta(t)$ (see Fig.2). Our simulations of droplets of water and glycerol-water mixture show that μ_f clearly affects the spreading dynamics as well as the shape of the droplet. For water droplets on steel $\mu_f \sim 0.52$Pa.s, while increasing its viscosity by introducing glycerol ($\mu_{\mathrm{l}} = 0.01$Pa.s) also increases $\mu_f \sim 0.72$Pa.s. These magnitudes for μ_f are in accordance with previous measurements on spontaneous spreading droplets ($V_i = 0$)[41]. Our simulations clearly show that μ_f controls the time scale for $\theta_{\mathrm{d}}(t)$ to approach the equilibrium angle, where $\theta_{\mathrm{d}}(t)$ is the droplets apparent contact angle, see Fig.2(b,d). It is noteworthy that the assumption of local equilibrium, i.e. equilibrium contact angle, over-predicts the spreading factor $\beta(t)$ and its maximum $\beta_{\max} = \max(\beta(t))$ for both liquids. Thus, to obtain agreement between the simulations and experiments we need to account for dissipation at the contact line and

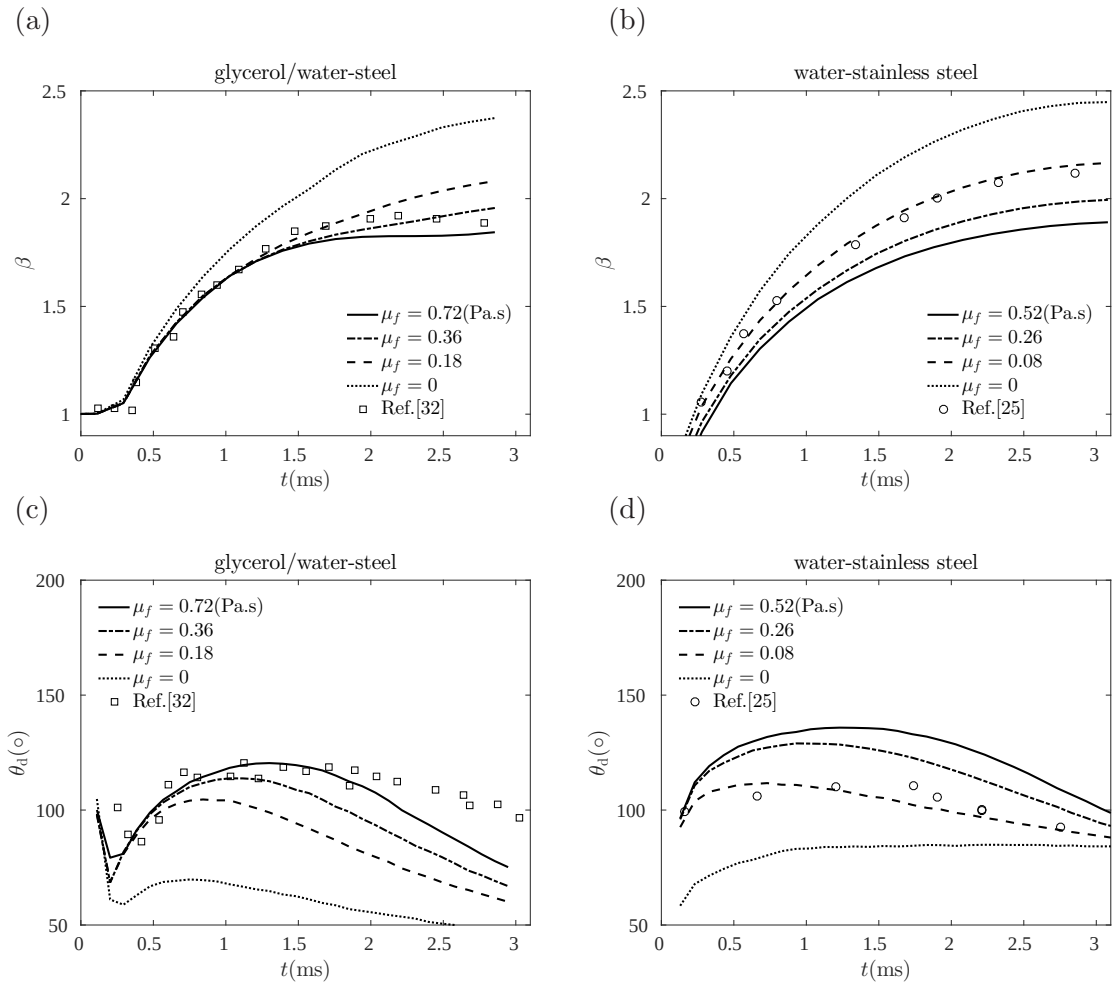

FIG. 2. Comparison of experimental data (markers) and numerical simulations (lines) for a droplet impacting onto smooth substrates with a speed $V_i = 1$m/s. Influence of (a-b) $\beta(t)$ and (c-d) $\theta_{\rm d}(t)$ as a function of the viscosity ($\mu_{\rm l}$) and the contact line friction parameter (μ_f), using the same definition of $\beta(t)$ as reported in experiments[32,35].

the local equilibrium assumption fails to capture the spatiotemporal droplet dynamics, see Fig.2(b,d).

After determining μ_f (Table 2) from an experiment for one impact speed V_i, we now assume μ_f to be a constant material parameter that must be independent of V_i. We challenge our hypothesis that μ_f is unique for a specific air-liquid-solid combination by directly comparing our simulations with experiments[32,35] for different $V_{\rm i}$. It is clear that as we increase $V_{\rm i}$ the droplets aspect ratio i.e. maximum height divided by $\beta_{\rm max}$, decreases at $\beta(t) = \beta_{\rm max}$. The simulated droplet shapes are in very good agreement with the experiments at $\beta_{\rm max}$,

TABLE II. Measurement of μ_f as a combination of air-liquid-solid combination.

liquid − substrate	$\theta_e(^\circ)$	μ_f (Pa·s)	*experiments*
glycerol/water-steel	52°	0.72	Ref.[32]
water-stainless steel	90°	0.08	Ref.[25]
water-steel	61°	0.52	Ref.[32]
water-aluminium	94°	0.08	Ref.[35]

where the difference in profiles (Fig.3(a) and (c-d)) is caused by the experimental side-view photos. Since the simulations show a slice through the droplet, they represent its actual shape. The dash-dot lines in panels to the right in Fig.3 illustrate how the shape of the droplet would look if we instead would have made a side-view image. Our simulations also capture the entrapment of an air bubble at the symmetry axis at the wall, as seen in Fig.3(a-c).

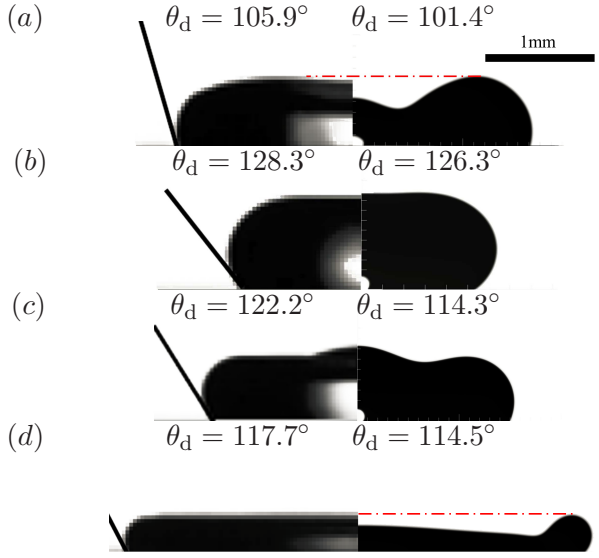

FIG. 3. Comparison of the experimental[32] (the left half, their Fig.2) and numerical (the right half) droplet shape as it impacts onto a steel substrate. (a) A water droplet (1 mPa.s) with $\mu_f = 0.52$Pa.s and $V_i = 0.57$m/s. (b-d) A glycerol-water droplet (10 mPa.s) with $\mu_f = 0.72$Pa.s and (b) $V_i = 0.28$m/s, (c) $V_i = 0.6$m/s, (d) $V_i = 1.86$m/s.

It is clear that μ_f needs to be determined individually for each air-liquid-substrate combination. A too small value for μ_f causes an over-prediction of $\beta_{\max}$, while a too large value for μ_f causes an under-prediction of $\beta_{\max}$, see Fig.4. We want to highlight that the value

for μ_f determined from a single experiment is also the best-fit for a range of impact speeds V_i and shows that μ_f is not a function of V_i.

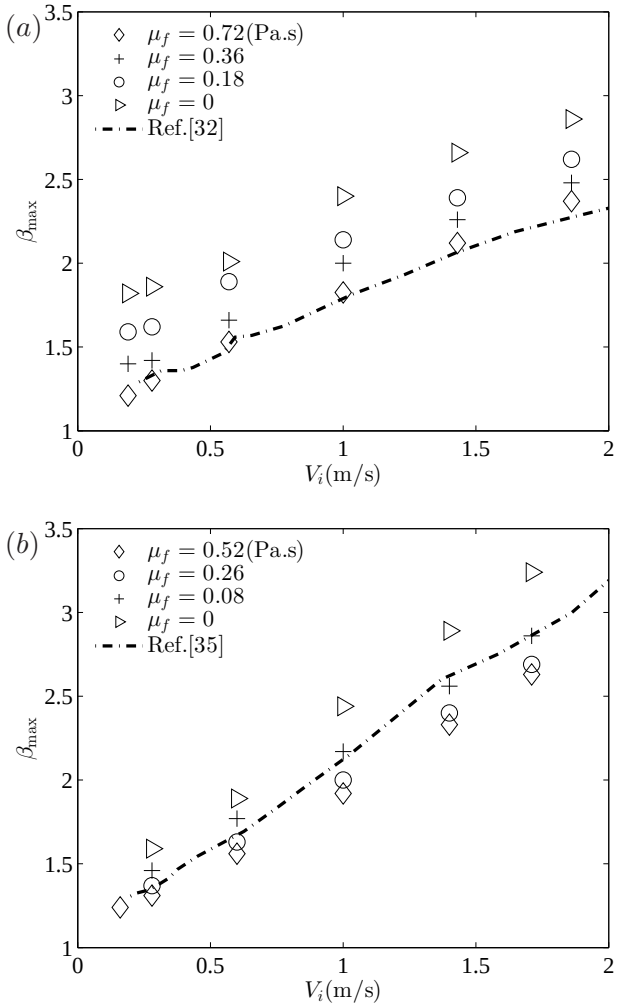

FIG. 4. The maximum spreading factor $\beta_{\max} = \max(\beta(t))$ as a function of impact speed V_i and μ_f. (a) Droplets with a glycerol-water mixture impacting onto a steel substrate, where the dashed line is interpolated experimental data[32] (their Fig.4). (b) Water droplets impacting onto an aluminum substrate, where the dashed line is interpolated experimental data[35] (their Fig.4(b)).

B. Droplet impact on textured substrates

Another parameter that can influence droplet spreading upon impact is the substrate topography[34,38]. For spontaneous spreading of droplets ($V_i = 0$) the friction factor μ_f has already been shown to rationalize spreading dynamics on rough substrates where the

magnitude of μ_f depends on the substrate roughness factor (S). To test if our description of the contact line dynamics can provide a universal framework that can effectively bridge impact dynamics on smooth and rough substrates, we test the relation for the effective contact line friction parameter $\mu_{\text{eff}} \sim S{\mu_f}^{51}$, having already estimated the value for μ_f for the smooth substrate. The geometry of the textured substrate gives the following roughness factor,

$$S = \frac{b + w - 2d\cos(\alpha) + 2d/\sin(\alpha)}{b + w}, \tag{6}$$

which is the ratio of the real area and projected area of the substrate. b, w, d, α are geometric parameters describing the grooved substrate, see inset in Fig.5. If the contact line friction parameter μ_f is known for the corresponding flat substrate, the effective friction μ_{eff} can easily be determined once the geometry of the micro-textured substrate is known.

We compare our simulations with experiments on substrates that have grooves along one direction with different aspect ratios. In Fig.5 the effective contact line friction parameter μ_{eff} is determined by matching the experimental data for the TS11 substrate[34] with a roughness factor $S_{11} = 1.27$, where we test the relation $\mu_{\text{eff}} \sim S{\mu_f}^{51}$ for the substrates TS140 ($S_{140} = 1.79$) and TS220 ($S_{220} = 2.45$)[34]. Although our assumption of axial-symmetry is slightly violated in the experiments, the linear relationship between S and μ_{eff} rationalizes β_{max} for the spreading perpendicular to the grooves. This is also believed to be the primary cause for the difference in μ_f found for a water droplet impacting on the smooth ($\mu_f = 0.08$Pa.s) and textured ($\mu_f = 0.28$Pa.s) stainless steel substrate.

C. Energy budget

Our results show that the local interface-wall contact line friction can affect the droplet impact dynamics, and we want next to determine its dissipative contribution and to compare it against the other primary contributions in the energy budget. To do this, we extract the different rates of energy and dissipations, where the principal contributions are; the rate of change of kinetic energy $R_\rho = \frac{1}{2}\int_\Omega \partial(\rho(C)\mathbf{u}^2)/\partial t \mathrm{d}\Omega$, the rate of viscous dissipation $R_\mu = \int_\Omega \mu(C)\left(\nabla\mathbf{u} + \nabla\mathbf{u}^{\mathbf{T}}\right) : \nabla\mathbf{u}\mathrm{d}\Omega$, and the rate of contact line dissipation $R_{\mu_f} = \int_\Gamma \epsilon\mu_f(\partial C/\partial t)^2\mathrm{d}\Gamma$. Ω is here the entire volume and Γ is the substrate area. In the droplet impact dynamics we observe that at early times $t^* < 0.25$ the magnitude of R^*_ρ decreases rapidly, while $R^*_{\mu_\mathrm{f}}$ on the other hand increases, see Fig.6. A minimum in R^*_ρ and

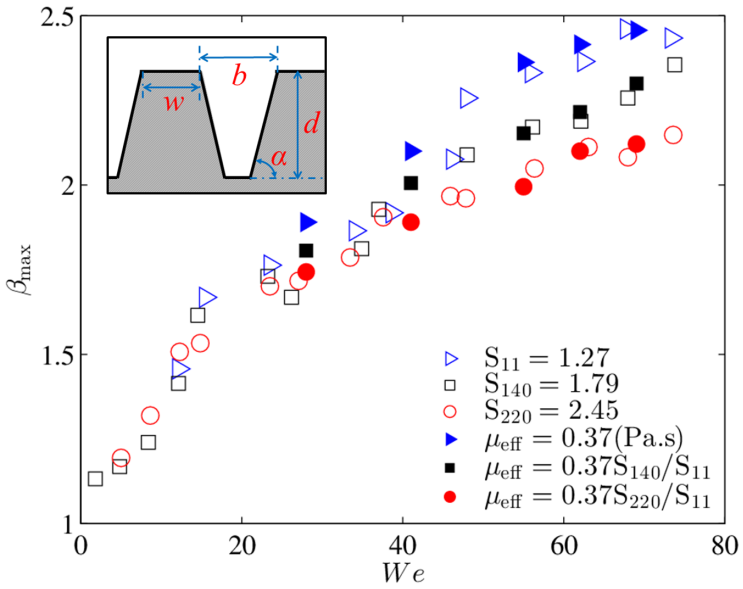

FIG. 5. $\beta_{\max}$ for water droplets impacting onto micro-textured stainless steel substrates with grooves along one direction (see inset). The filled markers are numerical simulations with $\mu_{\text{eff}} \sim S\mu_f$. The hollow markers are experimental results (Fig.3(b) in[34]). The inset shows the geometric parameters (w, b, d and α) for the grooved substrate (Fig.1 in[34]).

a maximum in $R^*_{\mu_f}$ take place at $t^* \approx 0.25$, whereas both slowly approach zero as the velocities decrease. Surprisingly, viscous dissipation appears to not play an important role in this regime as both $R^*_{\mu_f}$ and R^*_{ρ} are much larger for $\beta(t) < \beta_{\max}$.

D. Scaling laws for $\beta_{\max}(\mu_f)$

Since our simulations fall into both the inertia-viscous and the inertia-capillary regime, we can further test if our numerical simulations are also consistent with existing scaling laws. We compare our numerical data for $\mu_f = 0$ (Fig.7a) and the measured μ_f (Fig.7b) with another set of independent experimental data[23] for impacting droplets of different fluids. We use the scaling law for $\beta_{\max} = Re^{\frac{1}{5}} f(WeRe^{-\frac{2}{5}})$ that couples the inertia-viscous and inertia-capillary regime[22,23] and illustrated by the line in Fig.7. We see in Fig.7(a) that $\mu_f = 0$ creates results that deviate from the scaling law and the experiments. One exception is the simulations of water droplets, this is not surprising as the Reynolds number for water is ten times larger than for the glycerol-water mixture and inertial effects are therefore much more dominant. Including the effect of contact line dissipation by using the values for μ_f

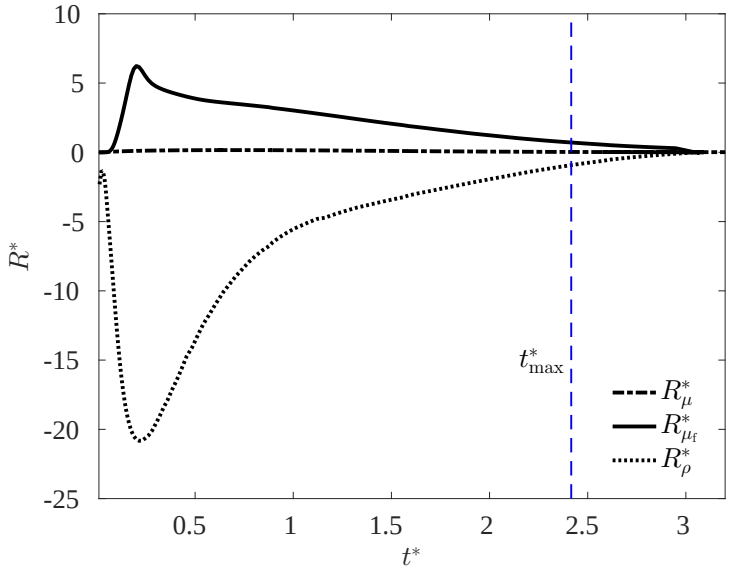

FIG. 6. The non-dimensional rate of change of kinetic energy ($R^*_\rho = \int_\Omega \frac{1}{2}Ca\frac{1}{2}Re\frac{\partial(\rho^*(C)\mathbf{u}^{*2})}{\partial t^*}\mathrm{d}\Omega$), rate of viscous dissipation ($R^*_\mu = \int_\Omega Ca\mu^*(C)\left(\nabla\mathbf{u}^* + \nabla\mathbf{u}^{*\mathbf{T}}\right) : \nabla\mathbf{u}^*\mathrm{d}\Omega$) and contact line dissipation ($R^*_{\mu_\mathrm{f}} = \int_\Gamma D_w\left(\frac{\partial C}{\partial t^*}\right)^2\mathrm{d}\Gamma$) for a glycerol-water droplet (10 mPa.s) impacting with; $V_i = 1\mathrm{m/s}, R = 0.92\mathrm{mm}$ and $\mu_f = 0.72\mathrm{Pa.s}$ i.e. $Re = 212, Ca = 0.15, We = 31.4$. $t^*_{\max} = 2.41$ is here the time in which the droplet is most deformed along r-direction $\beta_{\max} = 1.83$.

determined in Fig.2,4 makes the simulated data for $WeRe^{\frac{-2}{5}} > 1$ fit well with the scaling law $\beta_{\max} = Re^{\frac{1}{5}}f(WeRe^{-\frac{2}{5}})$ and the experiments. However, it is clear that for the regime where the effect from μ_f is expected to be important i.e. $WeRe^{\frac{-2}{5}} < 1$, both the experiments and the simulations deviate from the existing scaling law.

To improve the scaling prediction for $\beta_{\max}$ we include the influence from the contact line dissipation into the approximation for the energy balance,

$$\int_\Omega \frac{1}{2}\frac{\partial(\rho_\mathrm{l}\mathbf{u}^2)}{\partial t}\mathrm{d}\Omega \approx \int_\Omega \mu_\mathrm{l}\left(\nabla\mathbf{u} + \nabla\mathbf{u}^\mathbf{T}\right) : \nabla\mathbf{u}\mathrm{d}\Omega + \int_R \mu_f V_\mathrm{c}^2\mathrm{d}R + \int_s \sigma\frac{\partial s}{\partial t}\mathrm{d}s \qquad (7)$$

with the contact line speed defined as $V_\mathrm{c} = \partial R(t)/\partial t$. Note that the contact line dissipation is independent of the interface thickness and can be re-written[40] as $\int_\Gamma \epsilon\mu_f(\partial C/\partial t)^2\mathrm{d}\Gamma = \int_{R_c}\mu_f V_\mathrm{c}^2\mathrm{d}R_c$ with R_c as the radial position of the contact line. s is the droplet surface area and the last term on the right hand side of Eq.7 is the rate of change of droplet surface energy. Based on the approximated energy balance we assume the following scaling relations[31] for a droplet that has spread to $R_{\max}$ and has a height h; $\mathbf{u}^2 \sim V_\mathrm{i}^2$, $\nabla\mathbf{u} \sim V_\mathrm{i}/h$, $t \sim R_{\max}/V_\mathrm{i}$,

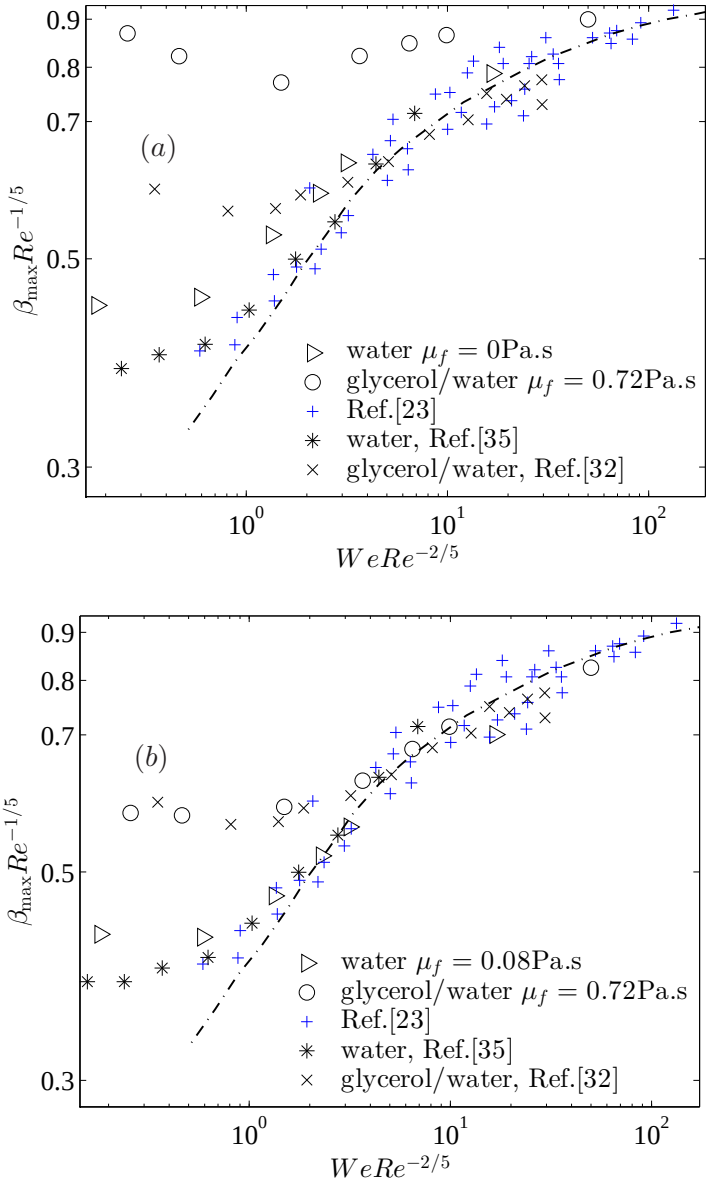

FIG. 7. The maximum spreading factor $\beta_{\max}$ for different liquids, from experiments[23,32,35] (symbols; $+, \times, *$) and simulations (hollow markers). The dashed line is illustrating[31] the scaling relation $\beta_{\max} = Re^{\frac{1}{5}} f(WeRe^{-\frac{2}{5}})$. (a) Comparing experiments[23,32,35] with numerical simulations for $\mu_f = 0$. (b)Comparing experiments[23,32,35] with numerical simulations for μ_f as reported Table 2.

$V_c \sim V_i$, $\Omega \sim R^3$, $\Gamma \sim R_{\max}$, $s \sim R_{\max}^2$. In addition mass conservation of the incompressible droplet demands that its volume remains constant and that $R^3 \sim hR_{\max}^2$. By introducing these scaling relations into Eq.7 we get the following expressions:

$$
\begin{aligned}
&\int_\Omega \frac{\partial(\rho_\mathrm{l}\mathbf{u}^2)}{\partial t}\mathrm{d}\Omega \sim \frac{\rho_\mathrm{l} V_\mathrm{i}^3 R^3}{R_\mathrm{max}} \\
&\int_\Omega \mu_\mathrm{l}\left(\nabla\mathbf{u} + \nabla\mathbf{u}^\mathbf{T}\right) : \nabla\mathbf{u}\mathrm{d}\Omega \sim \frac{\mu_\mathrm{l} V_\mathrm{i}^2 R_\mathrm{max}^4}{R^3} \\
&\int_\Gamma \mu_f V_\mathrm{c}^2 \mathrm{d}\Gamma \sim \mu_f V_\mathrm{i}^2 R_\mathrm{max} \\
&\int_s \sigma\frac{\partial s}{\partial t}\mathrm{d}s \sim \sigma V_\mathrm{i} R_\mathrm{max}.
\end{aligned}
\tag{8}
$$

Now substituting these scaling relations into Eq.(7) and rearranging the terms give β_max as a function of the contact line friction parameter μ_f,

$$
Re = \beta_\mathrm{max}^2\left(\frac{\mu_f}{\mu_\mathrm{l}} + \frac{1}{Ca} + \beta_\mathrm{max}^3\right). \tag{9}
$$

Three separate regimes appear, where we immediately see that the two limits $\frac{\mu_f}{\mu_\mathrm{l}} + \frac{1}{Ca} \ll \beta_\mathrm{max}^3$ ($\beta_\mathrm{max} \sim Re^{\frac{1}{5}}$) and $\frac{\mu_f}{\mu_\mathrm{l}} + \beta_\mathrm{max}^3 \ll \frac{1}{Ca}$ ($\beta_\mathrm{max} \sim We^{\frac{1}{2}}$) recovers the classical scaling laws. However, we identify a new regime for small and intermediate impact speeds i.e. $\frac{1}{Ca} + \beta_\mathrm{max}^3 \ll \frac{\mu_f}{\mu_\mathrm{l}}$ with $\beta_\mathrm{max} \sim (\mu_\mathrm{l} Re/\mu_f)^{\frac{1}{2}}$.To test this new scaling law we plot the data for $\mu_f/\mu_\mathrm{l} > 5(\beta_\mathrm{max}^3 + 1/Ca)$ from the simulations and experiments, which follows $\beta_\mathrm{max} \sim (Re\mu_\mathrm{l}/\mu_f)^{\frac{1}{2}}$, see Fig.8(a), instead of $\beta_\mathrm{max} \sim We^{\frac{1}{2}}$ or $\beta_\mathrm{max} \sim Re^{\frac{1}{5}}$, see Fig.8(b,c).

III. CONCLUSIONS

We have investigated the dynamics of droplets impacting onto solid substrates as a function of their viscosity, substrate wettability and substrate topography by deploying numerical simulations. By assuming linear response through a Stokes-like drag at the contact line, our simulations rationalize experimental observations for droplet impact on both smooth and rough substrates. Our results highlight that at low impact speeds the dissipation at the contact line needs to be included to predict the droplet spreading dynamics. We propose a scaling relation for this regime that is dominated by contact line dissipation $\beta_\mathrm{max} \sim (\frac{\mu_\mathrm{l}}{\mu_f} Re)^{\frac{1}{2}}$, complementing the classical scaling laws for β_max i.e. $\beta_\mathrm{max} \sim We^{\frac{1}{2}}$ and $\beta_\mathrm{max} \sim Re^{\frac{1}{5}}$ that are also identified in the numerical simulations. Moreover, our simulations highlight the link between substrate roughness and the effective contact line friction factor μ_eff that can provide a unifying framework to describe droplet impact dynamics.

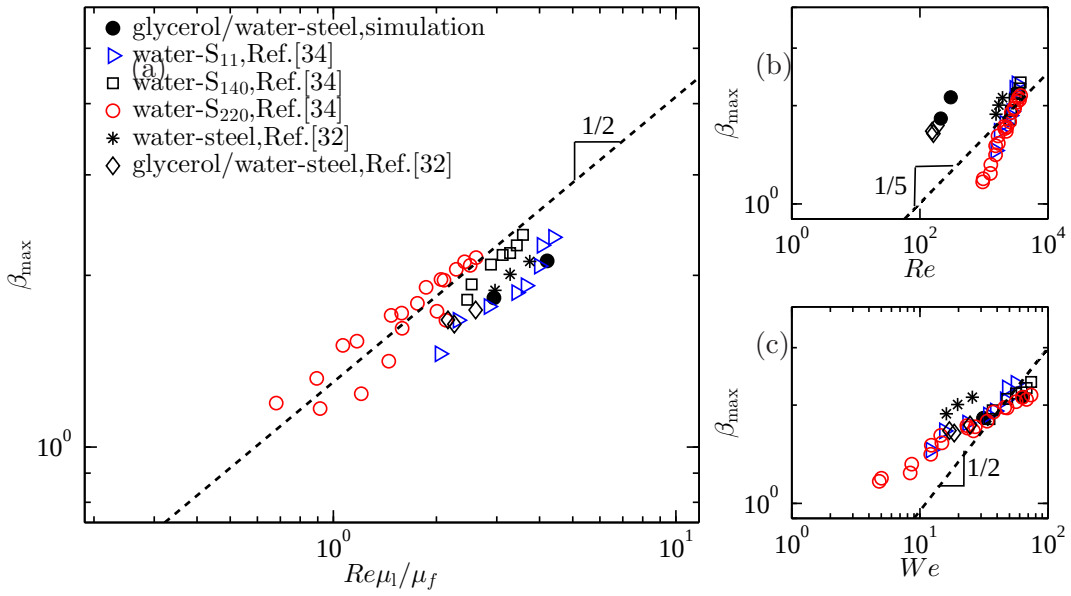

FIG. 8. Scalings for $\beta_{\max}$ with data from droplet impact on different substrates where $\frac{\mu_f}{\mu_l} > 5(\beta_{\max}^3 + \frac{1}{Ca})$. (a)$\beta_{\max}$ as a function of $\frac{\mu_l}{\mu_f}Re$. (b)$\beta_{\max}$ as a function of Re. (c) $\beta_{\max}$ as a function of We. Note that for the grooved substrates S_{11}, S_{140} and S_{220}, we use the measured valued for μ_{eff}.

REFERENCES

[1]R. Dykhuizen, "Review of impact and solidification of molten thermal spray droplets," Journal of Thermal Spray Technology **3**, 351–361 (1994).

[2]D. Attinger, Z. Zhao, and D. Poulikakos, "An experimental study of molten microdroplet surface deposition and solidification: transient behavior and wetting angle dynamics," Journal of Heat Transfer **122**, 544–556 (2000).

[3]S. Fathi, P. Dickens, and F. Fouchal, "Regimes of droplet train impact on a moving surface in an additive manufacturing process," Journal of Materials Processing Technology **210**, 550–559 (2010).

[4]V. Bergeron, D. Bonn, J. Y. Martin, and L. Vovelle, "Controlling droplet deposition with polymer additives," Nature **405**, 772–775 (2000).

[5]N. Z. Mehdizadeh, S. Chandra, and J. Mostaghimi, "Formation of fingers around the edges of a drop hitting a metal plate with high velocity," Journal of Fluid Mechanics **510**, 353–373 (2004).

[6]S. Mandre, M. Mani, and M. P. Brenner, "Precursors to splashing of liquid droplets on a solid surface," Physical Review Letters **102**, 134502 (2009).

[7]L. Duchemin and C. Josserand, "Curvature singularity and film-skating during drop impact," Physics of Fluids (1994-present) **23**, 091701 (2011).

[8]J. M. Kolinski, S. M. Rubinstein, S. Mandre, M. P. Brenner, D. A. Weitz, and L. Mahadevan, "Skating on a film of air: drops impacting on a surface," Physical Review Letters **108**, 074503 (2012).

[9]W. Bouwhuis, R. C. van der Veen, T. Tran, D. L. Keij, K. G. Winkels, I. R. Peters, D. van der Meer, C. Sun, J. H. Snoeijer, and D. Lohse, "Maximal air bubble entrainment at liquid-drop impact," Physical Review Letters **109**, 264501 (2012).

[10]Y. Liu, P. Tan, and L. Xu, "Compressible air entrapment in high-speed drop impacts on solid surfaces," Journal of Fluid Mechanics **716**, R9 (2013).

[11]C. W. Visser, P. E. Frommhold, S. Wildeman, R. Mettin, D. Lohse, and C. Sun, "Dynamics of high-speed micro-drop impact: numerical simulations and experiments at frame-to-frame times below 100 ns," Soft matter **11**, 1708–1722 (2015).

[12]E. Li and S. T. Thoroddsen, "Time-resolved imaging of a compressible air disc under a drop impacting on a solid surface," Journal of Fluid Mechanics **780**, 636–648 (2015).

[13]M. M. Driscoll and S. R. Nagel, "Ultrafast interference imaging of air in splashing dynamics," Physical Review Letters **107**, 154502 (2011).

[14]K. Yokoi, "Numerical studies of droplet splashing on a dry surface: triggering a splash with the dynamic contact angle," Soft Matter **7**, 5120–5123 (2011).

[15]C. W. Visser, Y. Tagawa, C. Sun, and D. Lohse, "Microdroplet impact at very high velocity," Soft matter **8**, 10732–10737 (2012).

[16]G. Riboux and J. M. Gordillo, "Experiments of drops impacting a smooth solid surface: A model of the critical impact speed for drop splashing," Physical Review Letters **113**, 024507 (2014).

[17]L. Xu, W. W. Zhang, and S. R. Nagel, "Drop splashing on a dry smooth surface," Physical Review Letters **94**, 184505 (2005).

[18]A. I. Fedorchenko, A.-B. Wang, and Y.-H. Wang, "Effect of capillary and viscous forces on spreading of a liquid drop impinging on a solid surface," Physics of Fluids (1994-present) **17**, 093104 (2005).

[19]I. V. Roisman, R. Rioboo, and C. Tropea, "Normal impact of a liquid drop on a dry surface: model for spreading and receding," in *Proceedings of the Royal Society of London A: Mathematical, Physical and Engineering Sciences*, Vol. 458 (The Royal Society, 2002) pp. 1411–1430.

[20]T. Bennett and D. Poulikakos, "Splat-quench solidification: estimating the maximum spreading of a droplet impacting a solid surface," Journal of Materials Science **28**, 963–970 (1993).

[21]G. Lagubeau, M. A. Fontelos, C. Josserand, A. Maurel, V. Pagneux, and P. Petitjeans, "Spreading dynamics of drop impacts," Journal of Fluid Mechanics **713**, 50–60 (2012).

[22]J. Eggers, M. A. Fontelos, C. Josserand, and S. Zaleski, "Drop dynamics after impact on a solid wall: theory and simulations," Physics of Fluids (1994-present) **22**, 062101 (2010).

[23]N. Laan, K. G. de Bruin, D. Bartolo, C. Josserand, and D. Bonn, "Maximum diameter of impacting liquid droplets," Physical Review Applied **2**, 044018 (2014).

[24]B. L. Scheller and D. W. Bousfield, "Newtonian drop impact with a solid surface," AIChE Journal **41**, 1357–1367 (1995).

[25]M. Pasandideh-Fard, Y. Qiao, S. Chandra, and J. Mostaghimi, "Capillary effects during droplet impact on a solid surface," Physics of Fluids (1994-present) **8**, 650–659 (1996).

[26]T. Mao, D. Kuhn, and H. Tran, "Spread and rebound of liquid droplets upon impact on flat surfaces," AIChE Journal **43**, 2169–2179 (1997).

[27]S. Chandra and C. Avedisian, "On the collision of a droplet with a solid surface," in *Proceedings of the Royal Society of London A: Mathematical, Physical and Engineering Sciences*, Vol. 432 (The Royal Society, 1991) pp. 13–41.

[28]D. Vadillo, A. Soucemarianadin, C. Delattre, and D. Roux, "Dynamic contact angle effects onto the maximum drop impact spreading on solid surfaces," Physics of Fluids (1994-present) **21**, 122002 (2009).

[29]C. Ukiwe and D. Y. Kwok, "On the maximum spreading diameter of impacting droplets on well-prepared solid surfaces," Langmuir **21**, 666–673 (2005).

[30]C. Clanet, C. Béguin, D. Richard, and D. Quéré, "Maximal deformation of an impacting drop," Journal of Fluid Mechanics **517**, 199–208 (2004).

[31]C. Josserand and S. Thoroddsen, "Drop impact on a solid surface," Annual Review of Fluid Mechanics **48**, 365–391 (2016).

[32]J. Lee, N. Laan, K. de Bruin, G. Skantzaris, N. Shahidzadeh, D. Derome, J. Carmeliet, and D. Bonn, "Universal rescaling of drop impact on smooth and rough surfaces," Journal of Fluid Mechanics **786**, R4 (2015).

[33]R. Kannan and D. Sivakumar, "Drop impact process on a hydrophobic grooved surface," Colloids and Surfaces A: Physicochemical and Engineering Aspects **317**, 694–704 (2008).

[34]V. Vaikuntanathan and D. Sivakumar, "Maximum spreading of liquid drops impacting on groove-textured surfaces: Effect of surface texture," Langmuir **32**, 2399–2409 (2016).

[35]J. B. Lee, D. Derome, R. Guyer, and J. Carmeliet, "Modeling the maximum spreading of liquid droplets impacting wetting and nonwetting surfaces," Langmuir **32**, 1299–1308 (2016).

[36]P. Tsai, S. Pacheco, C. Pirat, L. Lefferts, and D. Lohse, "Drop impact upon micro-and nanostructured superhydrophobic surfaces," Langmuir **25**, 12293–12298 (2009).

[37]R. C. van der Veen, M. H. Hendrix, T. Tran, C. Sun, P. A. Tsai, and D. Lohse, "How microstructures affect air film dynamics prior to drop impact," Soft matter **10**, 3703–3707 (2014).

[38]S. Robson and G. R. Willmott, "Asymmetries in the spread of drops impacting on hydrophobic micropillar arrays," Soft matter **12**, 4853–4865 (2016).

[39]A. Yarin, "Drop impact dynamics: splashing, spreading, receding, bouncing," Annual Review of Fluid Mechanics **38**, 159–192 (2006).

[40]A. Carlson, M. Do-Quang, and G. Amberg, "Dissipation in rapid dynamic wetting," Journal of Fluid Mechanics **682**, 213–240 (2011).

[41]A. Carlson, G. Bellani, and G. Amberg, "Contact line dissipation in short-time dynamic wetting," EPL (Europhysics Letters) **97**, 44004 (2012).

[42]D. Jacqmin, "Calculation of two-phase navier–stokes flows using phase-field modeling," Journal of Computational Physics **155**, 96–127 (1999).

[43]J. W. Cahn and J. E. Hilliard, "Free energy of a nonuniform system. i. interfacial free energy," The Journal of chemical physics **28**, 258–267 (1958).

[44]D. Jacqmin, "Contact-line dynamics of a diffuse fluid interface," Journal of Fluid Mechanics **402**, 57–88 (2000).

[45]P. Yue, C. Zhou, and J. J. Feng, "Sharp-interface limit of the cahn–hilliard model for moving contact lines," Journal of Fluid Mechanics **645**, 279–294 (2010).

[46]F. Magaletti, F. Picano, M. Chinappi, L. Marino, and C. M. Casciola, "The sharp-interface limit of the cahn–hilliard/navier–stokes model for binary fluids," Journal of Fluid Mechanics **714**, 95–126 (2013).

[47]G. Amberg, R. Tönhardt, and C. Winkler, "Finite element simulations using symbolic computing," Mathematics and Computers in Simulation **49**, 257–274 (1999).

[48]V. Khatavkar, P. Anderson, P. Duineveld, and H. Meijer, "Diffuse-interface modelling of droplet impact," Journal of Fluid Mechanics **581**, 97–127 (2007).

[49]Q. Zhang, T.-Z. Qian, and X.-P. Wang, "Phase field simulation of a droplet impacting a solid surface," Physics of Fluids (1994-present) **28**, 022103 (2016).

[50]Y. Wang, M. Do-Quang, and G. Amberg, "Events and conditions in droplet impact: a phase eld prediction," International Journal of Multiphase Flow **87**, 54–65 (2016).

[51]J. Wang, M. Do-Quang, J. J. Cannon, F. Yue, Y. Suzuki, G. Amberg, and J. Shiomi, "Surface structure determines dynamic wetting," Scientific reports **5**, 10–11 (2015).